Metal Double Layers with Sub-10 nm Channels

Thomas Siegfried,[†] Li Wang,[‡] Yasin Ekinci,[†] Olivier J.F. Martin,[§] and Hans Sigg[†,*]

[†]Laboratory for Micro- and Nanotechnology, Paul Scherrer Institut, 5232 Villigen-PSI, Switzerland, [‡]Eulitha AG, 5303 Würenlingen, Switzerland, and [§]Nanophotonics and Metrology Laboratory, EPFL, 1015 Lausanne, Switzerland

ABSTRACT Double-layer plasmonic nanostructures are fabricated by depositing metal at normal incidence onto various resist masks, forming an antenna layer on top of the resist post and a hole layer on the substrate. Antenna plasmon resonances are found to couple to the hole layer, inducing image charges which enhance the near-field for small layer spacings. For continued evaporation above the resist height, a sub-10 nm gap channel develops due to a self-aligned process and a minimal undercut of the resist sidewall. For such double layers with nanogap channels, the average surface-enhanced Raman scattering intensity is improved by a factor in excess of 60 in comparison to a single-layer antenna with the same dimensions. The proposed design principle is compatible with low-cost fabrication, straightforward to implement, and applicable over large areas. Moreover, it can be applied for any particular antenna shape to improve the signals in surface-enhanced spectroscopy applications.

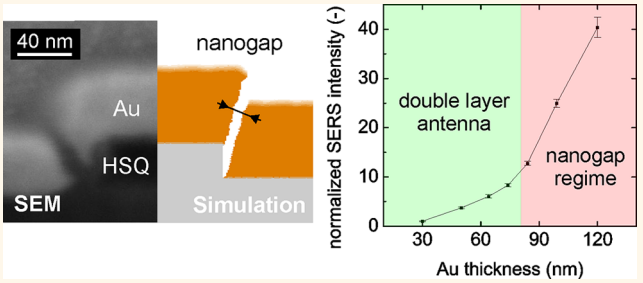

KEYWORDS: double layer · nanogap · SERS · antenna · coupled modes · surface plasmon · localized plasmon resonance · near-field

Surface-enhanced Raman spectroscopy enables promising applications in various fields including medical sensing, single-molecule detection, and electromagnetic field characterization.[1−3] Its extraordinary sensitivity relies on the near-field enhancement within electromagnetic hotspots, which are generated by the resonant modes of the electrons oscillating at the surface of noble metal nanoparticles.[4] In plasmonics, antenna geometries are commonly used due to their tunable plasmon resonance and efficient scattering to the far-field, enabling a good matching of the resonance with the excitation frequency and an efficient detection of the emitted waves, respectively.[4,5] Previously, antenna geometries were optimized to obtain strong near-field enhancement through, for example, the exploration of sharp particle edges, leading to strong field localization, or the utilization of particle pairs with few-nanometer gaps, leading to strongly coupled modes.[6−11] Strong near-field enhancement was also obtained with Fano resonant antenna geometries *via* the coupling to dark modes with suppressed absorption/scattering losses.[12−14] Apart from tuning the antenna geometry, the near-field enhancement can also be improved by placing the antenna onto a reflective layer with controlled spacing.[15−18] Thereby, not only coupling to the antenna resonance is improved but also the scattered field can be manipulated to steer the emission in the direction of detection.[19−22] Additionally, localized surface plasmon modes (LSPR) can be coupled to surface propagating plasmon modes (SPP) at the reflective layer, which may further improve the coupling to the incident field.[23−25] The total coupling efficiency of a particular antenna geometry used for surface-enhanced Raman spectroscopy (SERS) is also related to the density and surface coverage of the hotspots which in the above-mentioned examples were often very small. Dense antenna arrays with high average surface enhancement may thus be the better choice, provided that low-cost fabrication over large areas using only a few standard processing steps becomes available.[26] To date, the fabrication of the nanogap pattern is either based on randomly distributed particle assemblies and collapses[27,28] or requires high-resolution techniques[9] combined with multistep

* Address correspondence to hans.sigg@psi.ch.

Received for review January 20, 2014 and accepted March 11, 2014.

Published online March 11, 2014
10.1021/nn500375z

processes[29,30] that limit their widespread implementation and may not be adaptable for different pattern shapes.

Here we propose a straightforward single-step fabrication method to boost the near-field enhancement for various antenna patterns over large areas, by combining two established techniques, such as reflecting layers and nanogaps. Instead of isolated single-layer (SL) antenna geometries, we utilize double-layer (DL) antenna−hole pattern[15,17,31,32] obtained by metal evaporation onto a patterned photoresist. The nanogaps are added to the pattern by prolonged evaporation of the metal layer. When the metallic layer extends above the photoresist layer, an elongated sub-10 nm wide gap channel is formed as is predicted by our ballistic simulations. Our experiments reveal the enhanced near-field in DL pattern due to coupling of the antenna mode to image charges generated in the hole layer, and we expand the advantage of the DL pattern by combining them with the strong coupling in nanogaps.

RESULTS AND DISCUSSION

We start by comparing the plasmon resonances and near-field distribution in an isolated SL antenna pattern with a DL antenna of the same size, before we introduce the DL antennas with nanogap channels. Isolated antennas are fabricated by etching, while the corresponding DL structures are obtained *via* a simple single-step evaporation onto the same resist pattern previously used as etching mask, without further lift-off or etching processes. For the DL pattern, the metal on top of the resist post acts as an antenna and the metal film deposited on the substrate forms holes with shape of the inversed antenna and thus is representing the reflecting layer. The double-layer separation is determined by the resist height minus the metal layer thickness. We use ballistic simulations[8,33] to illustrate the cross section of SL (regime I) and DL antennas (regime II), shown in Figure 1a,b. Upon normal incidence deposition, the evaporated metal layer not only grows vertically but also slightly expands horizontally due to surface diffusion.[34] The apparent undercut in the top metal layer and the resist post leads to a shadowing of the metal layer that evolves at the substrate level. From this shadowing, a self-aligned nanometer spaced channel develops between the two metal layers as soon as the metal thickness deposited on the substrate exceeds the resist height (regime III), shown in Figure 1c. This channel is found to be the location where the antenna near-field localizes, and hence it is the origin for boosting the SERS enhancement as will be demonstrated below.

Let us first clarify the difference between the plasmon resonances of isolated SL antennas and DL antennas and show how this affects their near-field distribution. For their fabrication, we utilize extreme ultraviolet interference lithography[35] (EUV) to yield a triangular shaped antenna in a kagome array with a 700 nm lattice spacing, shown in Figure 2a,b for SL and DL antenna patterns, respectively.[36] The antenna thickness is 30 nm and much less than the height of the post, which is 90 nm. The diameter of the antenna is varied between 100 and 200 nm by altering the exposure time. Thereby, the plasmon resonance is shifted from 650 to 800 nm as is shown from the reflection spectra in Figure 2c and is confirmed by simulations using a surface integral approach (SIE)[37] in Figure 2d. SL antennas are fabricated using patterned PMMA resist posts as the etch mask, while the DL antennas of the similar dimensions are obtained by evaporation onto the same PMMA resist pattern. Both types of structures show a distinct resonance behavior with a peak in reflection for the isolated antenna pattern (Figure 2c) and a dip in reflection at the corresponding frequency for the DL antenna pattern (Figure 2e).

This reflection dip is verified by simulations (Figure 2f) and is explained by the lower metal layer acting as reflector. At resonance, the antenna couples to the incident field and induces a strong near-field at the metal/dielectric interface. This near-field is re-emitted into the far-field, leading to a reflection maximum. When such an antenna is placed in front of a reflector, the reflective layer dominates the reflection spectrum and the observed reflection dip originates from absorption and scattering at the plasmon resonance. The antenna near-field enhancement is probed by SERS after decorating the metal surface with a self-assembled benzene ethanethiol monolayer. As expected, the SERS intensity has an optimum under resonance matching conditions with the incident excitation λ_I at 633 nm and the analyzed Raman wavelength λ_R at 676 nm, shown in Figure 2g. The SERS intensity for the DL pattern is, as expected, stronger by a factor of 5. This phenomenon has also been observed for antennas on top of a continuous

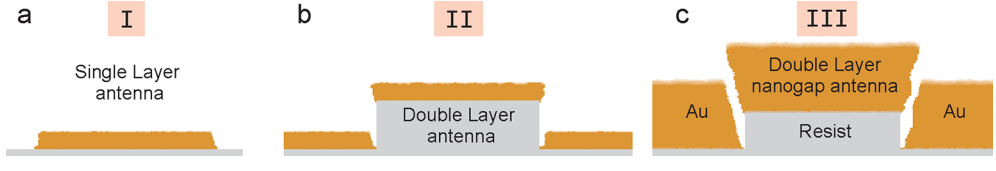

Figure 1. Ballistic simulation of the evaporated cross section for (a) single-layer antenna (I) after mask lift-off, (b) double-layer antenna pattern (II) separated by a resist post, and (c) double-layer pattern with a nanogap channel (III) for a metal layer thickness above the resist layer thickness.

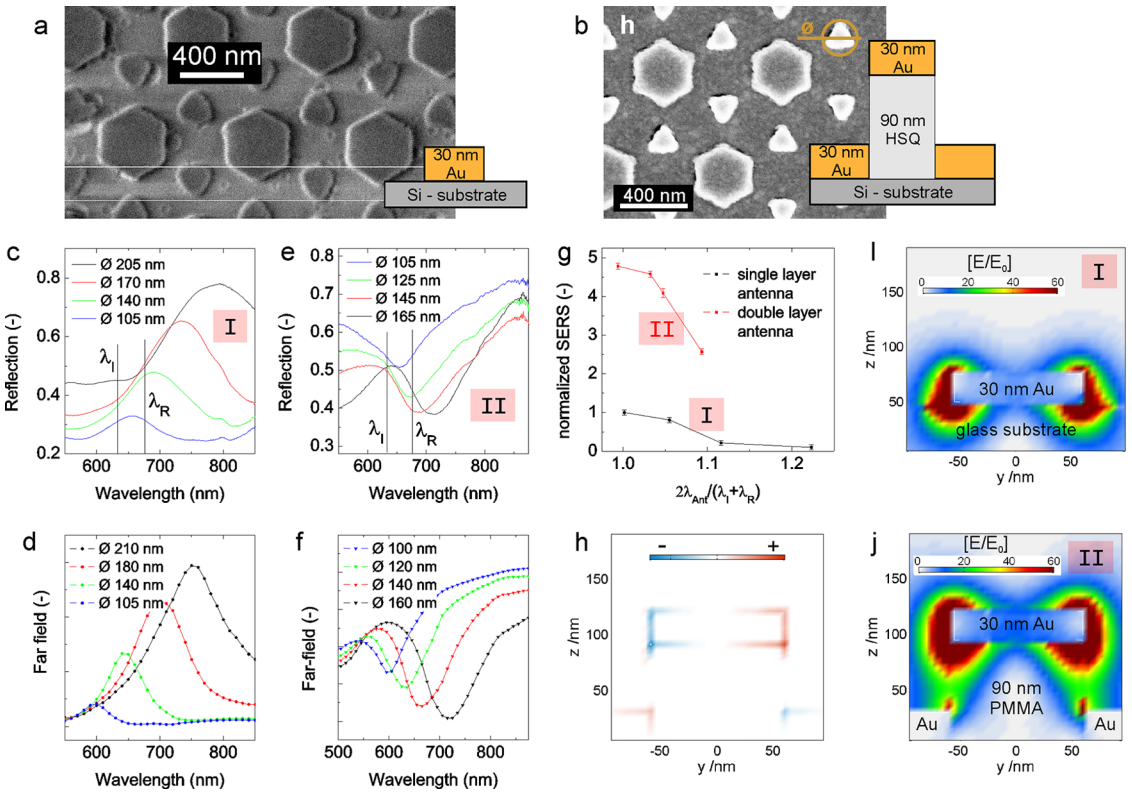

Figure 2. Comparison of 30 nm thick Au single-layer (I) and double-layer (II) antenna pattern. The substrate is silicon, and the 90 nm resist post is from PMMA. (a,b) SEM images of the triangular SL/DL antenna pattern, with a schematic of the cross section and the effective diameter approximation. (c,e) Reflection spectra of triangular SL/DL pattern with varying the effective diameter. The effective diameter corresponds to the diameter of a circle enclosing the triangular shape. The wavelengths of the 633 nm incident excitation λ_I and of the recorded Raman shift at 676 nm λ_R are marked. (d,f) Far-field simulation for an isolated SL/DL pattern with varying effective diameter. (g) SERS intensity of the 1008 cm^{-1} peak of a self-assembled benzene ethanethiol monolayer normalized to the maximal intensity of the SL antenna. The *x*-axis gives relative resonance position, normalized to the SERS excitation and emission wavelength. Best resonance matching is achieved for a value of 1. Error bars represent the standard deviation when mapping at 16 spatially separated spots. (h) Phase map of the near-field at resonance of a DL pattern covered by 30 nm Au film and (i,j) simulated near-field map at the resonance wavelength of 635 nm of a 30 nm thick Au antenna with 120 nm diameter in the SL/DL pattern, with 90 nm high PMMA resist post.

reflecting layer.[16,17,22,38] From the simulated phase of the near-field, we find image charges in the metal hole structure induced by the antenna on the resist post, as shown in Figure 2h. These image charges increase the near-field of the coupled antenna−hole mode above that one of the isolated antenna (Figure 2i,j), which in turn results in the enhanced SERS signals.

Next, we discuss the signal improvements from narrowing the gap, which is formed between the upper and lower metal layers at increased metal layer thicknesses. Similarly, the layer spacing could also be varied by the resist thickness. In the above used PMMA layers, the upper and lower metal levels are found to coalesce as soon the metal thickness exceeds the height of the posts because of an overcut of the resist sidewall.[35] The plasmon mode and near-field intensity thereby are quenched.[38] The overcut of positive tone resists is characteristic in EUV lithography and results from absorption at the exposure wavelength of 13.5 nm, leading to lower doses at larger resist skin depths. In turn, when we switch to the negative tone resist hydrogen silsesquioxane (HSQ), a distinct undercut of the resist layers is obtained. This effect is found to be crucial for the generation of a self-aligned nanogap channel, as shown for grating structures with a period of 250 nm and a line width of 125 nm (Figure 3). Corresponding SL Au gratings are obtained using the same evaporated mask for a subsequent lift-off process.

We observe localized resonances in reflection for the individual grating lines at a wavelength of 600 nm for a 30 nm thick SL and with the electric field polarized perpendicular to the grating lines (cf. Figure 3a). Similar to the antenna pattern in Figure 2, the reflection maximum inverts to a reflection dip when we switch to a DL grating with same line width and layer thickness, as shown in Figure 3a. With increasing Au thickness, the localized plasmon resonance in the DL strongly broadens. This broadening is accurately described by the far-field simulations shown in Figure 3b and is ascribed to an increased coupling of the hole and antenna layer as the spacing decreases. In parallel,

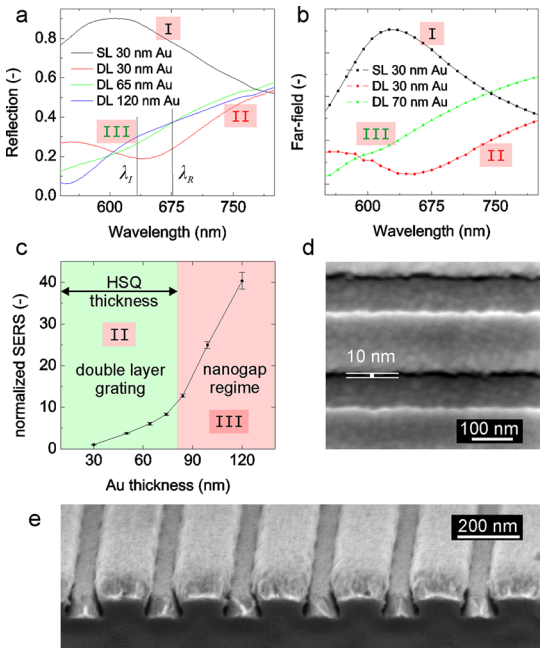

Figure 3. Double-layer Au gratings at various metal layer thicknesses. The substrate is glass; the resist is 90 nm HSQ, and the grating period is 250 nm with a duty cycle of 0.5. (a) Reflection spectra. The wavelengths of the 633 nm incident excitation λ_I and of the recorded Raman shift at 676 nm λ_R are marked. The numbers I, II, and III specify the pattern regime of SL, DL, and DL antenna with nanogaps. (b) Far-field simulation. (c) SERS intensity of the 1008 cm^{-1} peak of a self-assembled benzene ethanethiol monolayer normalized to the intensity of the 30 nm DL grating. Error bars represent the standard deviation when mapping 16 spatially separated spots. (d,e) Scanning electron micrograph (SEM) of a 120 nm thick gold metal DL. The substrate is tilted by 16° (d) and cleaved (e) to see the nanogap channel.

the SERS intensity is steadily increasing for smaller DL spacings (Figure 3c). We can relate the SERS signal to the antenna's near-field enhancement by accounting for the number density of contributing molecules: When the DL grating thickness is increased from 30 to 64 nm, the exposed surface area and hence the analyte number increases by roughly 1.4. At the same time, the SERS intensity gains by a factor of 6 (cf. Figure 3c), which we translate to a SERS activity enhancement of >4.

Above a metal thickness of 80 nm, the DL nanogap regime is formed, where we find vertically elongating nanogap channels (Figure 3d), as it was simulated in Figure 1. The formation of the DL nanogap channels is accompanied by a sharp increase in the SERS signal, which further rises for even longer channel lengths (Figure 3c). This gain in SERS results from strong localization of the plasmon mode in the nanochannel, which results in extremely high near-fields as will be shown in the next section. The continued rise in the SERS signal for prolonged nanogap channels can have multiple origins, such as the reduction of the gap size for larger metal thicknesses, the spatial elongation of the near-field hotspot area, or the additional formation of gap plasmons.[7] Overall, we find a 40-fold increased SERS activity for the roughly 10 nm spaced DL grating (120 nm metal thickness) of elongated nanogap channels in comparison to a 50 nm spaced DL grating (30 nm metal thickness). We calculate an area averaged SERS enhancement factor (EF) of roughly 3×10^6 for the 120 nm thick Au DL grating by comparing the SERS intensity at monolayer analyte coverage to the Raman intensity of pure benzene ethanethiol analyte, which is liquid at room temperature. The analyte number density in SERS is given by the focal spot area and the packing density of an analyte monolayer, and in the case of the Raman event, it is given by the density, molar mass, and focal spot volume of the pure analyte liquid.[39] This average SERS EF value is similar to what we have previously reported on periodic sub-10 nm gap resonator arrays.[8] This hints that DL nanogap gratings can have a similar sensing efficiency as sub-10 nm gap arrays, although the fabrication of the DL pattern is considerably simpler to implement. Here we would also like to note that the DL nanogap fabrication is a robust process even for larger metal thicknesses leading to vertically elongated sub-10 nm gap channels. The high yield in accuracy over large areas is seen from SEM images (Figure 3d,e) and confirmed by the low SERS standard deviation of 3% for mapping across the patterned area (Figure 3c). This excellent standard deviation consistently prooves that the nanochannel gap size is homogeneous across the pattern and that there are only few spots of DL coalescence quenching the near-field hotspot. The latter can be seen from the SEM images in Figures 3 and 4, with additional large area images given in Figure S1 of the Supporting Information. Although we use a unique high-resolution technique to fabricate our resist pattern, the DL evaporation process is also applicable to a resist pattern obtained from low-cost lithography, such as self-assembled nanospheres.[38] The only requirement is that the resist sidewall needs to have an undercut to prevent coalescence of the two metal layers upon deposition. One advantage of our method is that there is potentially no height limit of the nanogap channel length because of the shadowing effect. This shadowing averts coalescence of the gap as long as the metal surface diffusion is low. Furthermore, the gap size of the nanochannel can be controlled by varying the resist layer thickness, as found in ballistic simulations shown in Figure S2 of the Supporting Information.

In the next section, we expand the DL nanogap fabrication method to arbitrary antenna shapes to prove its general validity. This we demonstrate on a kagome lattice of oval shaped antennas fabricated on an 90 nm thick HSQ layer, shown in Figure 4e. The antennas are sized 200 × 320 nm with a lattice spacing of 700 nm and result in LSPR peaks above 800 nm wavelengths for 30 nm thick isolated SL gold antennas (not shown). The reflection of the DL antenna pattern holds traces of the isolated SL resonance in the form of

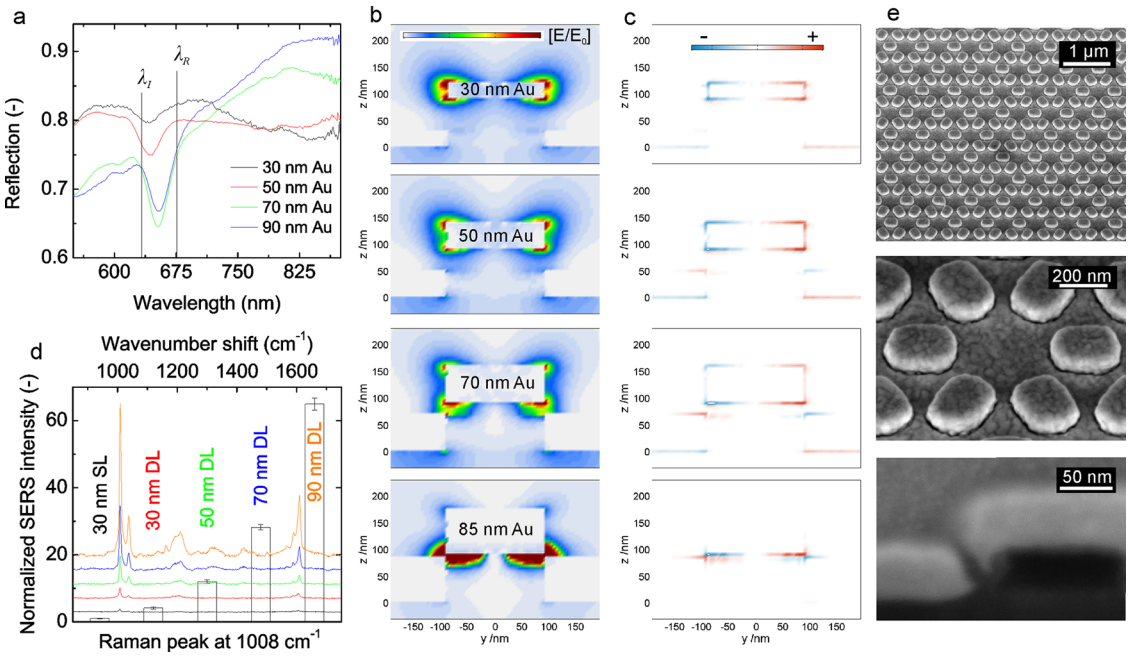

Figure 4. Double-layer oval shaped antennas arranged in a hexagonal lattice, with increasing metal layer thickness and layer spacing, respectively. The substrate is silicon; the resist is 90 nm of HSQ; the antenna size is roughly 200 × 300 nm, and the period is 700 nm. (a) Reflection spectra. The wavelengths of the 633 nm incident excitation λ_I and of the recorded Raman shift at 676 nm λ_R are marked. (b,c) Near-field intensity/near-field phase plots for DL antenna with Au thickness between 30 and 90 nm. The near-field and phase are plotted at the resonance wavelength of the pattern, which is 690 nm. (d) SERS spectra (with arbitrary units) and the SERS intensity of the 1008 cm^{-1} peak of a self-assembled benzene ethanethiol monolayer normalized to the intensity of the 30 nm single-layer antenna pattern. Error bars represent the standard deviation when mapping 16 spatially separated spots. (e) SEM images of a 90 nm Au DL antenna pattern. The cross section SEM was cut by FIB and is recorded at an angle of 55°; hence the vertical axis is shrunk by a factor of roughly 0.6.

a broad reflection dip at wavelengths above 750 nm, as seen in Figure 4a and as has been discussed for the previous pattern. Additionally, we observe a weak but narrow dip at around 650 nm, which matches with the Raman excitation and emission. With increasing metal thickness and hence reduced DL spacing, the resonance at 650 nm gains in magnitude, while the isolated antenna LSPR dip shifts to wavelengths above 750 nm. On the basis of this observation and in analogy with earlier results obtained for similar double-layer geometries,[25] we attribute the resonance at 650 nm to a coupled mode consisting of the LSPR of the antenna and the continuous metal layer beneath. The slight decrease in the measured resonance dip for the 90 nm thick DL pattern might result from sporadically appearing spots where the nanogap coalesces and/or is related to the fact that the near-field distribution is modified when a nanogap is formed, shown in the following. Since our simulation tool does not support kagome lattice boundary conditions and enlarging the simulation unit cell would be computationally too expensive, we perform simulations for a rectangular arranged antenna−hole double-layer pattern to illustrate the dependency of coupled modes on the spacing between both layers when the nanogap is formed. Because of this simplification, the resonance in the calculation appears at 690 nm (not shown) and not at the observed 650 nm. However, we expect that the mode characteristics are well-described, nevertheless. Indeed, from the near-field simulations, shown in Figure 4b, we find a coupled resonance when a nanogap starts to form for thicknesses larger than 70 nm. The corresponding image charges in the hole layer are evident from the phase maps of Figure 4c. The coupling strength increases for small layer spacings, leading to the extreme near-field enhancement in the gap region (cf. the bottom image of Figure 4b). The near-field dependence for increasing metal thickness is nicely confirmed by SERS showing a 60-fold signal enhancement of the nanogap DL pattern coated by a 90 nm Au layer in comparison to the similarly shaped but only 30 nm thick SL antenna, shown in Figure 4d. For the 90 nm thick DL pattern, we obtain an area averaged SERS EF of 1×10^7, which is larger than the EF of the previously discussed grating DL pattern, in spite of the higher nanogap density in the latter. This extraordinary EF may be the result from improved coupling efficiency to the incident field because of the distinct plasmon resonance, which matches so well with the SERS excitation (Figure 4a). For the grating DL pattern, only a broad resonance is observed in reflection (cf. Figure 3a).

CONCLUSION

We demonstrated a straightforward, single-step fabrication method for double-layer antenna patterns

with sub-10 nm spacing, where SERS is enhanced up to 60-fold in comparison to an isolated single-layer antenna pattern. By direct metal evaporation onto a photoresist pattern, antenna−hole metal double layers were obtained, where the antenna plasmon mode can couple to image charges in the hole layer. A self-limiting sub-10 nm channel between both metal layers is found to develop for resist layers with an undercut. Such patterns combine the advantages of far-field coupling of antennas, the performance enhancement by light recycling in reflecting double layers, and the extreme near-field enhancement in sub-10 nm gaps. The simple fabrication technique can be implemented for a broad range of patterns aiming at increasing the enhancement factor in surface-enhanced spectroscopy with applications such as single-molecule studies or other fields requiring extremely large and homogeneous field intensities over large areas.

METHODS

Fabrication of the Pattern. Extreme ultraviolet interference lithography at the Swiss Light Source[40] is used to expose grating masks at a wavelength of 13.5 nm in 90 nm thick resist layers of hydrogen silsesquioxane (HSQ) or polymethyl methacrylate (PMMA). Line patterns are obtained from a two-beam interference mask leading to a period of 250 nm over a patterned area of 1 mm^2. Kagome patterns are obtained from a multibeam interference mask with a lattice spacing of 700 nm over a patterned area 100 × 100 μm^2.[36] HSQ is developed in a 25% tetramethylammonium hydroxide (TMAH) solution for 60 s, and PMMA is developed in a 20% isopropyl alcohol/water mixture for 45 s.

SL antenna patterns are obtained by etching into a Au layer. A glass substrate is evaporated with 1 nm Cr, 30 nm Au, and again 25 nm Cr, before a 50 nm PMMA or HSQ layer is patterned. The resist pattern serves as a mask for the following reactive ion etching process based on Cl_2/CO_2 plasma to remove the 25 nm Cr layer. The obtained Cr pattern then serves as a hard mask to remove the 30 nm Au layer by ion etching in Ar/SF_6 plasma. The Au antennas are then cleaned from the remaining Cr mask in a Cr etching bath.

SL gratings are obtained by evaporation through a PMMA/HSQ resist mask. The 100 nm PMMA and 80 nm HSQ are spun on a glass wafer. After development of the top HSQ layer, the PMMA film is under etched in an O_2 plasma. The metal grating (1 nm Cr, 30 nm Au) is then evaporated thermally, and the resist pattern is removed in an acetone bath under gentle sonication.

DL gratings and antenna patterns are obtained by direct evaporation onto a 90 nm thick PMMA or HSQ resist layer. The substrate was silicon, and thermal evaporation was done at normal incidence with a 1 nm Cr adhesion layer, thereby minimizing near-field quenching.[41] Nanogap channels could only be obtained from HSQ layers, due to the apparent resist undercut, which prevents the coating of the resist sidewall and eventually suppresses the coalescence of the layers.

Optical Measurements. Reflection spectra are recorded with a Sentech spectrometer connected to a Leica microscope. The incident field is focused through a 20× (0.45 NA) objective and is unpolarized for the kagome pattern and polarized for the grating pattern with the electric field across the lines. The reflection spectrum from a continuous Au layer on the same substrate served as the reference.

SERS experiments are performed on a Horiba LabRam HR with a grating resolution of 600 lines mm^{-1}. The excitation source (HeNe laser, 633 nm) with an incident power of 2 mW is focused (50×, 0.5 NA) and laterally deflected within an area of 10 × 10 μm^2 to suppress photobleaching. The incident field is linearly polarized with the electric field aligned across the grating lines. The average of 16 single spectra is taken over a patterned area of 800 × 400 μm^2 for the grating pattern and 80 × 80 μm^2 for the kagome pattern in order to allow for statistical evaluation. The SERS intensities correspond to the Raman peak of the 1008 cm^{-1} vibrational mode from a self-assembled benzene ethanethiol monolayer obtained by 12 h immersion in a 1 mM solution.

Numerical Simulations. Ballistic Monte Carlo simulations are performed to analyze the cross section of the metal evaporation process.[33] Using a 2D homemade code, the trajectory and sticking of single metal particles sized at 0.5 nm are simulated. Particles are impinging under normal incidence from random positions. Once a particle reaches the uppermost surface, surface diffusion of particles is modeled with a diffusion length of 2 nm in order to fill empty pores within this distance.

The far-field spectra, near-field amplitude, and phase maps are calculated with a full-field numerical method based on the solution of surface integral equations (SIE).[37] The permittivities for Si, PMMA, and Cr are taken from an online database.[42] The refractive index of glass and HSQ are estimated with 1.5 and 1.39, respectively;[43] the permittivity of Au was estimated with values from Johnson & Christy,[44] and the surrounding medium was air. The antenna and grating geometries are discretized using a triangular mesh with a maximum side length of 20 nm. The simulation of the grating pattern is carried out in a 3D unit cell with periodic boundary conditions along the line plane of 100 nm depth and across the line plane of 250 nm width. The substrate is glass, and the resist is HSQ. The polarization of the electric field is set across the lines. The simulation of the isolated and DL pattern is carried out in a quadratic lattice with a period of 500 nm and periodic boundary conditions. While isolated antennas are discretized with a triangular shape, the DL pattern is approximated with a circular shape of corresponding diameter. The substrate is glass for the SL pattern and Si for the DL pattern with PMMA as the resist. The simulation of the DL oval antennas is carried out in a quadratic lattice with a period of 500 nm and periodic boundary conditions. The polarization of the electric field is set across the short axis of the antenna.

Conflict of Interest: The authors declare no competing financial interest.

Acknowledgment. We thank the Swiss National Science Foundation (SNF) for financial support. Part of this work was performed at the Swiss Light Source, Paul Scherrer Institute, Switzerland.

Supporting Information Available: Large area SEM images of double-layer grating and antenna pattern with nanogap channels; ballistic simulations of double-layer pattern with varying resist thickness, showing the control over the gap size. This material is available free of charge *via* the Internet at http://pubs.acs.org.

REFERENCES AND NOTES

1. Qian, X. M.; Peng, X. H.; Ansari, D. O.; Yin-Goen, Q.; Chen, G. Z.; Shin, D. M.; Yang, L.; Young, A. N.; Wang, M. D.; Nie, S. M. *In Vivo* Tumor Targeting and Spectroscopic Detection with Surface-Enhanced Raman Nanoparticle Tags. *Nat. Biotechnol.* **2008**, *26*, 83–90.
2. Kneipp, K.; Wang, Y.; Kneipp, H.; Perelman, L. T.; Itzkan, I.; Dasari, R. R.; Feld, M. S. Single Molecule Detection Using Surface-Enhanced Raman Scattering (SERS). *Phys. Rev. Lett.* **1997**, *78*, 1667–1670.
3. Bukasov, R.; Ali, T. A.; Nordlander, P.; Shumaker-Parry, J. S. Probing the Plasmonic Near-Field of Gold Nanocrescent Antennas. *ACS Nano* **2010**, *4*, 6639–6650.
4. Halas, N. J.; Lal, S.; Chang, W.-S.; Link, S.; Nordlander, P. Plasmons in Strongly Coupled Metallic Nanostructures. *Chem. Rev.* **2011**, *111*, 3913–3961.

5. Le, F.; Brandl, D. W.; Urzhumov, Y. A.; Wang, H.; Kundu, J.; Halas, N. J.; Aizpurua, J.; Nordlander, P. Metallic Nanoparticle Arrays: A Common Substrate for Both Surface-Enhanced Raman Scattering and Surface-Enhanced Infrared Absorption. *ACS Nano* **2008**, *2*, 707–718.
6. Zuloaga, J.; Prodan, E.; Nordlander, P. Quantum Description of the Plasmon Resonances of a Nanoparticle Dimer. *Nano Lett.* **2009**, *9*, 887–891.
7. Siegfried, T.; Ekinci, Y.; Martin, O. J. F.; Sigg, H. Gap Plasmons and Near-Field Enhancement in Closely Packed Sub-10 nm Gap Resonators. *Nano Lett.* **2013**, *13*, 5449–5453.
8. Siegfried, T.; Ekinci, Y.; Solak, H. H.; Martin, O. J. F.; Sigg, H. Fabrication of Sub-10 nm Gap Arrays over Large Areas for Plasmonic Sensors. *Appl. Phys. Lett.* **2011**, *99*, 263302.
9. Duan, H.; Hu, H.; Kumar, K.; Shen, Z.; Yang, J. K. W. Direct and Reliable Patterning of Plasmonic Nanostructures with Sub-10-nm Gaps. *ACS Nano* **2011**, *5*, 7593–7600.
10. Theiss, J.; Pavaskar, P.; Echternach, P. M.; Muller, R. E.; Cronin, S. B. Plasmonic Nanoparticle Arrays with Nanometer Separation for High-Performance SERS Substrates. *Nano Lett.* **2010**, *10*, 2749–2754.
11. Chen, X.; Park, H.-R.; Pelton, M.; Piao, X.; Lindquist, N. C.; Im, H.; Kim, Y. J.; Ahn, J. S.; Ahn, K. J.; Park, N.; *et al.* Atomic Layer Lithography of Wafer-Scale Nanogap Arrays for Extreme Confinement of Electromagnetic Waves. *Nat. Commun.* **2013**, *4*, 2361.
12. Ye, J.; Wen, F.; Sobhani, H.; Lassiter, J. B.; Dorpe, P. V.; Nordlander, P.; Halas, N. J. Plasmonic Nanoclusters: Near Field Properties of the Fano Resonance Interrogated with SERS. *Nano Lett.* **2012**, *12*, 1660–1667.
13. Gallinet, B.; Siegfried, T.; Sigg, H.; Nordlander, P.; Martin, O. J. F. Plasmonic Radiance: Probing Structure at the Angstrom Scale with Visible Light. *Nano Lett.* **2012**, *13*, 497–503.
14. Luk'yanchuk, B.; Zheludev, N. I.; Maier, S. A.; Halas, N. J.; Nordlander, P.; Giessen, H.; Chong, C. T. The Fano Resonance in Plasmonic Nanostructures and Metamaterials. *Nat. Mater.* **2010**, *9*, 707–715.
15. Min, Q.; Pang, Y.; Collins, D. J.; Kuklev, N. A.; Gottselig, K.; Steuerman, D. W.; Gordon, R. Substrate-Based Platform for Boosting the Surface-Enhanced Raman of Plasmonic Nanoparticles. *Opt. Express* **2011**, *19*, 1648–1655.
16. Seok, T. J.; Jamshidi, A.; Kim, M.; Dhuey, S.; Lakhani, A.; Choo, H.; Schuck, P. J.; Cabrini, S.; Schwartzberg, A. M.; Bokor, J.; *et al.* Radiation Engineering of Optical Antennas for Maximum Field Enhancement. *Nano Lett.* **2011**, *11*, 2606–2610.
17. Shoute, L. C. T. Multilayer Substrate-Mediated Tuning Resonance of Plasmon and SERS EF of Nanostructured Silver. *ChemPhysChem* **2010**, *11*, 2539–2545.
18. Hou, Y.; Xu, J.; Zhang, X.; Yu, D. SERS on Periodic Arrays of Coupled Quadrate-Holes and Squares. *Nanotechnology* **2010**, *21*, 195203.
19. Ahmed, A.; Gordon, R. Directivity Enhanced Raman Spectroscopy Using Nanoantennas. *Nano Lett.* **2011**, *11*, 1800–1803.
20. Ahmed, A.; Gordon, R. Single Molecule Directivity Enhanced Raman Scattering Using Nanoantennas. *Nano Lett.* **2012**, *12*, 2625–2630.
21. Zhu, W.; Wang, D.; Crozier, K. B. Direct Observation of Beamed Raman Scattering. *Nano Lett.* **2012**, *12*, 6235–6243.
22. Wang, D.; Zhu, W.; Chu, Y.; Crozier, K. B. High Directivity Optical Antenna Substrates for Surface Enhanced Raman Scattering. *Adv. Mater.* **2012**, *24*, 4376–4380.
23. Chu, Y.; Zhu, W.; Wang, D.; Crozier, K. B. Beamed Raman: Directional Excitation and Emission Enhancement in a Plasmonic Crystal Double Resonance SERS Substrate. *Opt. Express* **2011**, *19*, 20054–20068.
24. Christ, A.; Zentgraf, T.; Tikhodeev, S. G.; Gippius, N. A.; Martin, O. J. F.; Kuhl, J.; Giessen, H. Interaction between Localized and Delocalized Surface Plasmon Polariton Modes in a Metallic Photonic Crystal. *Phys. Status Solidi B* **2006**, *243*, 2344–2348.
25. Lévêque, G.; Martin, O. J. F. Optical Interactions in a Plasmonic Particle Coupled to a Metallic Film. *Opt. Express* **2006**, *14*, 9971–9981.
26. Natan, M. J. Concluding Remarks Surface Enhanced Raman Scattering. *Faraday Discuss.* **2006**, *132*, 321–328.
27. Strobel, S.; Sperling, R. A.; Fenk, B.; Parak, W. J.; Tornow, M. Dielectrophoretic Trapping of DNA-Coated Gold Nanoparticles on Silicon Based Vertical Nanogap Devices. *Phys. Chem. Chem. Phys.* **2011**, *13*, 9973–9977.
28. Schmidt, M. S.; Hubner, J.; Boisen, A. Large Area Fabrication of Leaning Silicon Nanopillars for Surface Enhanced Raman Spectroscopy. *Adv. Mater.* **2012**, *24*, Op11–Op18.
29. Chen, X. S.; Park, H. R.; Pelton, M.; Piao, X. J.; Lindquist, N. C.; Im, H.; Kim, Y. J.; Ahn, J. S.; Ahn, K. J.; Park, N.; *et al.* Atomic Layer Lithography of Wafer-Scale Nanogap Arrays for Extreme Confinement of Electromagnetic Waves. *Nat. Commun.* **2013**, *4*, 2361.
30. Zhu, W. Q.; Banaee, M. G.; Wang, D. X.; Chu, Y. Z.; Crozier, K. B. Lithographically Fabricated Optical Antennas with Gaps Well below 10 nm. *Small* **2011**, *7*, 1761–1766.
31. Li, W.-D.; Ding, F.; Hu, J.; Chou, S. Y. Three-Dimensional Cavity Nanoantenna Coupled Plasmonic Nanodots for Ultrahigh and Uniform Surface-Enhanced Raman Scattering over Large Area. *Opt. Express* **2011**, *19*, 3925–3936.
32. Li, W. D.; Hu, J.; Chou, S. Y. Extraordinary Light Transmission through Opaque Thin Metal Film with Subwavelength Holes Blocked by Metal Disks. *Opt. Express* **2011**, *19*, 21098–21108.
33. Müller-Pfeiffer, S.; van Kranenburg, H.; Lodder, J. C. A Two-Dimensional Monte Carlo Model for Thin Film Growth by Oblique Evaporation: Simulation of Two-Component Systems for the Example of Co−Cr. *Thin Solid Films* **1992**, *213*, 143–153.
34. Subramanian, S.; Catchmark, J. M. Molecular Ruler Lithography Using Sacrificial Host Structures Fabricated Using Electron Beam Lithography. *J. Micro/Nanolithogr., MEMS, MOEMS* **2006**, *5*, 049701.
35. Auzelyte, V.; Dais, C.; Farquet, P.; Grutzmacher, D.; Heyderman, L. J.; Luo, F.; Olliges, S.; Padeste, C.; Sahoo, P. K.; Thomson, T.; *et al.* Extreme Ultraviolet Interference Lithography at the Paul Scherrer Institut. *J. Micro/Nanolithogr., MEMS, MOEMS* **2009**, *8*, 021204-10.
36. Wang, L.; Terhalle, B.; Guzenko, V. A.; Farhan, A.; Hojeij, M.; Ekinci, Y. Generation of High-Resolution Kagome Lattice Structures Using Extreme Ultraviolet Interference Lithography. *Appl. Phys. Lett.* **2012**, *101*, 093104-5.
37. Gallinet, B.; Kern, A. M.; Martin, O. J. F. Accurate and Versatile Modeling of Electromagnetic Scattering on Periodic Nanostructures with a Surface Integral Approach. *J. Opt. Soc. Am. A* **2010**, *27*, 2261–2271.
38. Wen, X.; Xi, Z.; Jiao, X.; Yu, W.; Xue, G.; Zhang, D.; Lu, Y.; Wang, P.; Blair, S.; Ming, H. Plasmonic Coupling Effect in Ag Nanocap-Nanohole Pairs for Surface-Enhanced Raman Scattering. *Plasmonics* **2013**, *8*, 225–231.
39. Siegfried, T.; Kind, M.; Terfort, A.; Martin, O. J. F.; Zharnikov, M.; Ballav, N.; Sigg, H. Reusable Plasmonic Substrates Fabricated by Interference Lithography: A Platform for Systematic Sensing Studies. *J. Raman Spectrosc.* **2012**, *44*, 170–175.
40. Päivänranta, B.; Langner, A.; Kirk, E.; David, C.; Ekinci, Y. Sub-10 nm Patterning Using EUV Interference Lithography. *Nanotechnology* **2011**, *22*, 375302.
41. Siegfried, T.; Ekinci, Y.; Martin, O. J. F.; Sigg, H. Engineering Metal Adhesion Layers That Do Not Deteriorate Plasmon Resonances. *ACS Nano* **2013**, *7*, 2751–2757.
42. Li, X.; Hu, H.; Li, D.; Shen, Z.; Xiong, Q.; Li, S.; Fan, H. J. Ordered Array of Gold Semishells on TiO_2 Spheres: An Ultrasensitive and Recyclable SERS Substrate. *ACS Appl. Mater. Interfaces* **2012**, *4*, 2180–2185.
43. Yang, C.-C.; Chen, W.-C. The Structures and Properties of Hydrogen Silsesquioxane (HSQ) Films Produced by Thermal Curing. *J. Mater. Chem.* **2002**, *12*, 1138–1141.
44. Johnson, P. B.; Christy, R. W. Optical Constants of the Noble Metals. *Phys. Rev. B* **1972**, *6*, 4370–4379.